A Long Short-Term Memory Network for Vessel Reconstruction Based on Laser Doppler Flowmetry via a Steerable Needle

Vani Virdyawan and Ferdinando Rodriguez y Baena, *Member, IEEE*

***Abstract*— Hemorrhage is one risk of percutaneous intervention in the brain that can be life-threatening. Steerable needles can avoid blood vessels thanks to their ability to follow curvilinear paths, although knowledge of vessel pose is required. To achieve this, we present the deployment of laser Doppler flowmetry (LDF) sensors as an *in-situ* vessel detection method for steerable needles. Since the perfusion value from an LDF system does not provide positional information directly, we propose the use of a machine learning technique based on a Long Short-term Memory (LSTM) network to perform vessel reconstruction online. Firstly, the LSTM is used to predict the diameter and position of an approaching vessel based on successive measurements of a single LDF probe. Secondly, a "no-go" area is predicted based on the measurement from four LDF probes embedded within a steerable needle, which accounts for the full vessel pose. The network was trained using simulation data and tested on experimental data, with 75% diameter prediction accuracy and 0.27 mm positional Root Mean Square (RMS) Error for the single probe network, and 77% vessel volume overlap for the 4-probe setup.**

***Index Terms*— Laser Doppler flowmetry, vessel reconstruction, percutaneous intervention, steerable needle, machine learning, long short-term memory (LSTM).**

I. Introduction

PERCUTANEOUS intervention procedures are particularly favourable in minimally invasive neurosurgery, due to the delicate and complex nature of the nervous system and the need to leave surrounding healthy neural tissue unharmed [1]. These are routinely performed for biopsies [2], deep brain stimulation (DBS) [3], and direct drug infusion to the brain, such as in convection-enhanced delivery (CED) [4]. During any one of these procedures, the needle must avoid blood vessels, since puncturing one can pose a life-threatening complication. Before surgery, the surgeon thus chooses a vessel-free insertion path based on pre-operative imaging data. However, this form of pre-operative planning cannot eliminate the risk of bleeding due to the existence of intra-operative brain shift and the limited imaging resolution [5], [6]. During DBS implantation, for instance, hemorrhage can occur in up to 5% of cases [7].

To prevent bleeding related to vessel puncture, real-time, light-based imaging modalities embedded within the tip of a surgical needle have been proposed. These imaging modalities use optical fibres to deliver the laser/light to, and collect reflect light from the tissue. The use of optical fibres allows the probe to be small, such that it can be included within a surgical needle. For instance, both forward and side viewing Optical Coherence Tomography (OCT) imaging has been used for vessel detection during needle insertion [8], [9]. Additionally, a simplified version of OCT, called Coherence-Gated Doppler (CGD), has also been implemented, which however does not provide quantitative information about the vessel location [10]. During DBS implantation, Wårdell *et al.* [11] proposed the use of Laser Doppler Flowmetry (LDF) as a vessel detection sensor. Side viewing probes are mainly used for vessel detection during biopsy procedures. These include interstitial optical tomography and remission spectroscopy [12], [13].

The aforementioned systems were embedded in rigid needles. Since the insertion path of a rigid needle is limited to a straight path, if a vessel is detected along the insertion path, the procedure must be interrupted. This limitation is driving the development of a flexible needle that can be steered to follow a curvilinear path. One such steerable needle design is the Programmable Bevel-Tip Needle (PBN), which is specifically designed to access deep lesions inside the brain [14]. PBNs offer a multi-segment design (Fig. 1a), which is inspired by the egg laying channel of parasitic wasps. Each PBN segment has an interlocking mechanism that links it to adjacent segments, while allowing for axial sliding. During needle insertion, the axial offset between segments creates a bending moment at the needle tip, which can be controlled and adjusted dynamically during the insertion process. By varying the offset, the bending radius and insertion direction can be controlled, enabling the needle to be steered [15]. Using a steerable needle, the procedure can continue even if a vessel is detected, as a new insertion path to the target can be generated 'on the fly', without the need for a full needle retraction. For this to be possible, however, information about vessel pose (position and orientation) is required to provide

Manuscript received June 18, 2019; revised August 2, 2019; accepted August 6, 2019. Date of publication August 8, 2019; date of current version November 13, 2019. This work was supported in part by the European Union's EU Research and Innovation programme Horizon 2020 under Grant agreement 688279 and in part by the Imperial Confidence in Concepts - Joint Translational Fund through EPSRC Impact Acceleration Account and MRC Confidence in Concept Scheme. The associate editor coordinating the review of this article and approving it for publication was Prof. Danilo Demarchi. *(Corresponding author: Ferdinando Rodriguez y Baena.)*

The authors are with the Department of Mechanical Engineering, Imperial College London, London SW7 2AZ, U.K. (e-mail: v.virdyawan14@imperial.ac.uk; f.rodriguez@imperial.ac.uk).

Digital Object Identifier 10.1109/JSEN.2019.2934013

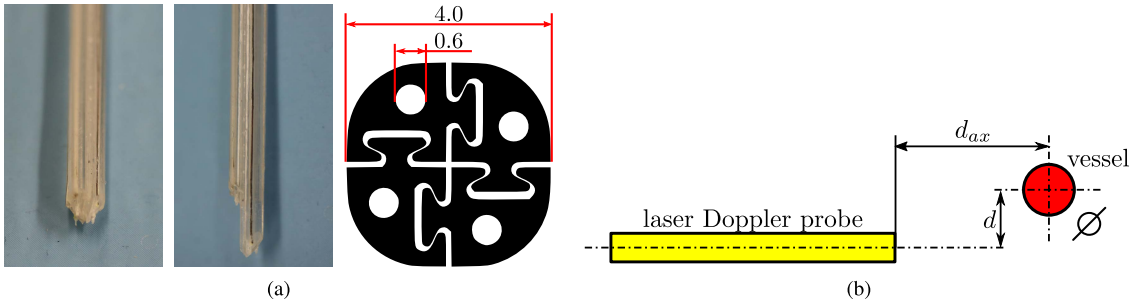

Fig. 1. a) Left: the 4 mm PBN with all of the segments aligned; middle: the PBN with offset introduced into the needle; right: the cross section of the PBN, which has a diameter of 4 mm and four, 0.6 mm outer diameter working channels. b) Axial distance d_{ax} and off-axis distance d from the tip of the LDF probe to a vessel with a diameter ∅.

the necessary knowledge to plan and execute a subsequent avoidance strategy.

In [16], we performed a feasibility study by embedding a forward-looking sensor within two of the PBN segments. Each sensor was located parallel but offset to the central needle axis (see Fig. 1a). A commercial LDF system was chosen, with a few millimetres off-axis detection range. The LDF sensor detects a vessel by measuring the Doppler shift effect in the light refracted by moving blood cells flowing within it. Since a perfusion value corresponds to many vessel positions, in [16], successive measurements combined with a look-up table (measured under controlled conditions with varying parameters) of the inverse perfusion value were used to estimate the axial (d_{ax}) and off-axis (d) distance from the tip of the Doppler probe to a vessel (Fig. 1b). However, this method only works for a given pair of tissue and vessel properties (e.g. a 0.6 mm vessel diameter with 5 mm/s flow rate).

In three-dimensional space, many vessel poses can have the same pair of off-axis and axial distances from a given Doppler probe. In [16], we used the measurements of two LDF probes to reduce the possibility of vessel pose ambiguity. The off-axis distance was used to generate a detection circle for each probe. Using tangent lines between two detection circles (one for each probe), vessel poses were reduced to four. Subsequently, in [17], we investigated the use of four LDF sensors to improve vessel pose prediction. Relative measurements from four probes were exploited to classify a "no-go" region in front of the needle. Relative measurements were exploited to normalize the results so that the classification could be performed for any set of tissue optical properties. However, there are several limitations in the algorithm presented in [17]. It cannot be used to predict vessel diameter or the axial distance d_{ax} from the vessel to the Doppler probe, and it is assumed that the vessel lies on a plane perpendicular to the insertion axis. These represent important shortcomings, which we address in this work.

Under real conditions, neither the vessel nor the tissue properties are known beforehand. Hence, in this article, a Long Short-Term Memory (LSTM) network is employed to infer information about vessel pose based on successive LDF probe measurements, where no prior knowledge of the scene is required. The perfusion values recorded while the needle is inserted into the tissue are considered as sequential data to feed the network, and full needle pose is estimated by exploiting the mutual information available within the time sequence. Since a relative offset between segments is required to steer the PBN, it is not possible to ascertain which of the segments tips will detect a vessel first. Consequently, laser Doppler probes were embedded in each of the needle segments such that, as a vessel approaches any one segment, its presence can be detected and an estimate of vessel position and diameter can be made [17]. Once detected, all PBN segments are aligned and measurements from all laser Doppler probes are exploited to predict the full vessel pose.

This article consists of two main sections. Firstly, Section II investigates the ability of the LSTM network to predict diameter, axial distance, and off-axis distance of a vessel based on successive measurements *from a single LDF probe*. Secondly, Section III discusses the development of the LSTM network to directly predict the "no-go" area inferred from successive measurements from *four LDF probes* embedded within a prototype PBN. The results are then discussed in Section IV, with conclusions and a summary in Section V.

II. Single Probe Vessel Detection

A. Materials and Methods

LSTMs require a large number of training data sets, which would be impractical to acquire experimentally, as in [17]. Therefore, a Monte-Carlo simulation was performed to model measurements from an LDF system [18], [19]. The detection fibre was modelled using a ring detector (see Fig. 2) [20]. In each run, the simulation was stopped if there were 100,000 photons detected in the detector. The detail of the method to compute the perfusion value from the simulation is explained in [20]. The simulations were compared to the characterization results for a 0.6 mm diameter vessel phantom with 20 mm/s flow velocity, acquired with the phantom set-up described in [17].

The simulation was then extended to model the perfusion value for 0.3, 0.6, and 0.9 mm diameter vessels, with reduced scattering coefficient (μ_s') equal to 0.55, 0.75, and 0.95 mm^{-1}. The flow velocities were arbitrarily set at 10, 15, and 20 mm/s, which are values in the range of biological blood flow in smaller vessels. For each set of optical properties, the perfusion values were simulated at off-axis positions ranging from 0 to 2 mm in 0.2 mm increments and at axial positions ranging between 0.75 mm and 4.05 mm, in 0.3 mm increments.

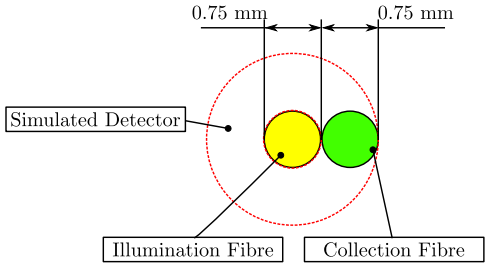

Fig. 2. Schematic diagram of the detector that was used in the simulation.

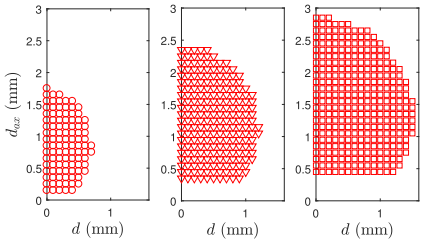

Fig. 3. Detection area of the laser probe for each vessel diameter. Left: 0.3 mm diameter vessel, middle: 0.6 mm diameter vessel, right: 0.9 mm diameter vessel.

For each vessel diameter, the maximum and the minimum simulated perfusion value at a certain vessel position from the probe tip were recorded. These maximum and minimum data were subsequently used in the form of a look-up table. To generate training data sets, the perfusion value for a certain vessel diameter at a given position was generated based on a random number uniformly distributed between the maximum and the minimum perfusion value at that point. The uniformly distributed perfusion value assumption means that the probabilities for μ_s' and the vessel flow velocity were uniform. Gaussian noise with zero mean was subsequently added to the generated perfusion value to simulate the shape of a real signal. The standard deviation used for the Gaussian noise was obtained from the characterization results in [17]. A perfusion value between simulated positions was approximated using a two-dimensional interpolation.

LSTM networks use the previous state at time $t-1$ with the current data point as an input for the network [21]. Therefore, it can capture the long-term dependencies hidden within sequential data. In this section, the LSTM network was used to predict the probability of vessel parameters $V(\varnothing, d_{ax}, d)$ based on perfusion measurements $Perf_1, Perf_2, Perf_3, \ldots, Perf_t$. Mathematically, this is equivalent to computing:

$$P(V(\varnothing, d_{ax}, d) \mid Perf_1, Perf_2, \ldots, Perf_t) \tag{1}$$

To obtain a value for the probability in equation 1, the measurement range of the sensors was discretized with 0.1 mm resolution for three vessel diameters (0.3, 0.6, and 0.9 mm). One set of parameters in the discretized element $(\varnothing, d_{ax}, d)$ represents an output class of the network. The problem then becomes that of a multi-class classification. The mean perfusion value in the absence of a vessel was 28 AU, with a standard deviation of 8 AU. The perfusion limit for a detected vessel was then set at 55 AU (the mean perfusion value in the absence of a vessel plus three times its standard deviation). Using this perfusion limit, there were 659 classes where the vessel was inside the detection range of the probe. By adding the no-detection class (ND), the total number of classes was 660. Fig. 3 shows a comparison of the probe detection range for each vessel diameter.

The hyper-parameters of the LSTM network were chosen manually: the number of layers was empirically set to 2, with 100 cells in each layer [22]. To prevent over-fitting, a drop-out with a value of 0.5 was used [23]. At the output layer, softmax was used to predict the probability of each class, so that:

$$P_i = \frac{e^{z_i}}{\sum_{j=1}^{K} e^{(z_j)}} \tag{2}$$

where P_i is the probability of class i, z_i is the output value of class i, and K is the total number of classes. Vessel parameters $(\varnothing, d_{ax}, d)$ were chosen based on the class with the highest probability. The network was trained by minimizing the cross entropy between the prediction output and the output of the training data set.

The training data set consisted of 30,000 sequences, with 30 positions in each series. 3,000 sequences were generated for validation, and another 3,000 were generated for testing. Since the minimum radius of curvature for the PBN prototype was experimentally measured to be 70 mm and the maximum d_{ax} that can be detected by the sensor is only ≈ 2 mm, the insertion was modelled as a straight line (i.e. with no change in d between successive positions). This is because the error introduced (≈ 0.03 mm) by this approximation falls below the resolution used to discretize the sensor detection range (≈ 0.1 mm). In the insertion simulation, at first a class was chosen randomly. The chosen class was then located randomly at one out of thirty possible positions between 0 and 8.7 mm away from the needle tip. At this location, the position of the vessel was modified by addition of a uniformly distributed random value between -0.05 - 0.05 mm (equal to the resolution of the class) in both d_{ax} and d. The probe was moved forward with 0.3 mm increments if $d_{ax} \geq \frac{\varnothing}{2} + 0.3$ mm. At the first instance where $d_{ax} < \frac{\varnothing}{2} + 0.3$ mm the probe was either: moved forwards, backwards, or stopped, until the 30^{th} position was reached, at which point the simulation was terminated.

Since the movement direction of the probe is used as an additional training parameter, the input of the network was set to be:

$$\left[Perf_t \ \mathbf{F}^\top\right]^\top \tag{3}$$

where $Perf_t$ is the perfusion at time t, and $\mathbf{F}^\top$ is a 3×1 vector that defines the movement direction of the probe, with

$$\mathbf{F} = \begin{cases} \begin{bmatrix} 1 & 0 & 0 \end{bmatrix}, & \text{if the probe is moving backwards} \\ \begin{bmatrix} 0 & 1 & 0 \end{bmatrix}, & \text{if the probe is stopping} \\ \begin{bmatrix} 0 & 0 & 1 \end{bmatrix}, & \text{if the probe is moving forwards} \end{cases} \tag{4}$$

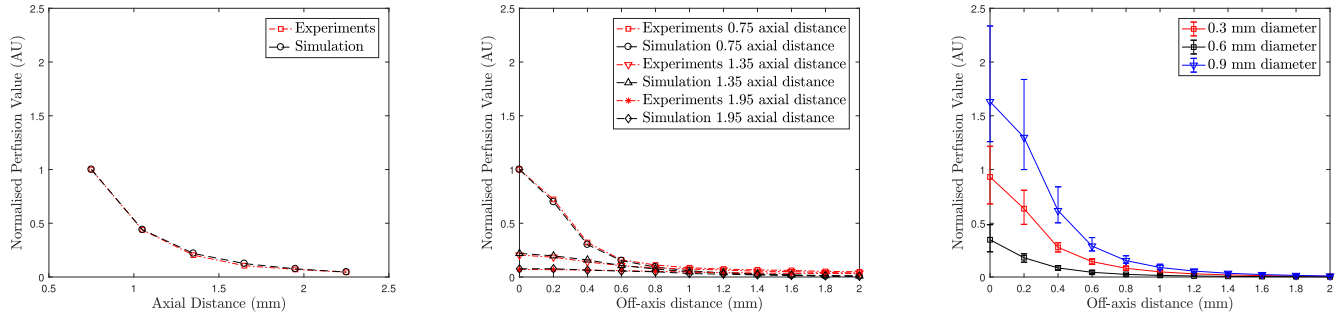

Fig. 4. a) Comparison of the axial normalized perfusion value between experiments (dash-dot line) and simulation (dash-line) at 0 mm off-axis position. b) Comparison of the off-axis normalized perfusion value between experiments (dash-dot line) and simulation (dash-line) at three axial distances: 0.75 mm, 1.35 mm, and 1.95 mm. c) The error-bar shows the maximum and minimum perfusion values for each vessel diameter at 0.75 mm axial distance, with varying tissue optical properties and flow velocity rates.

The generated training data set has an imbalance distribution. To train the network, a cost matrix to penalize the loss from a class with a higher number of samples (i.e. a higher frequency of occurrence) was used [24]. The misclassification cost of class i ($C[i,i]$) was thus defined as:

$$C[i,i] = \left(\frac{1}{n_i}\right)^{\gamma} \tag{5}$$

where n_i is the number of samples in class i, and $\gamma \in [0,1]$ is a trade-off parameter.

The performance of the network was evaluated using a confusion matrix. The confusion matrix classifies the prediction into four categories: true positive (t_p), true negative (t_n), false positive (f_p), and false negative (f_n). Since the dataset is highly imbalanced, the following evaluation metrics were used to evaluate the ability of the network to correctly detect the presence of a vessel inside the detection range of the sensor [24]:

$$\text{Precision} = \frac{\sum t_p}{\sum (t_p + t_n)} \tag{6}$$

$$\text{Recall} = \frac{\sum t_p}{\sum (t_p + f_n)} \tag{7}$$

$$F_1 = 2 \cdot \frac{\text{Precision} \cdot \text{Recall}}{\text{Precision} + \text{Recall}} \tag{8}$$

The confusion matrix was then used to investigate the network performance in predicting each vessel diameter using the test data set generated in simulation. It was also used to obtain the optimum γ value by training the network for 1,000 epochs while the value of γ was set to a number between 0 and 1, in 0.1 increments. We found that the optimum γ was 0.4. Finally, the network was used to predict the vessel parameters for real insertion experiments, where successive measurements from the insertion experiments in [17] were used to evaluate the performance of the trained network. The network was programmed in Python using the TensorFlow LSTM library.

B. Results

Fig. 4a and 4b show a comparison between the simulated and measured perfusion values. To ease comparison, all perfusion values were normalized against the perfusion value at 0.75 mm axial and 0.00 mm off-axis distance. The simulation shows good agreement with the experiments. The main focus of vessel detection in a steerable needle system is to obtain information about its pose and diameter. Therefore, the extended simulation results were used to show the possible range of perfusion values given a vessel diameter and position, with variable tissue optical properties and flow velocity rates. Fig. 4c shows these perfusion ranges for each vessel diameter at 0.75 mm axial distance.

TABLE I

CONFUSION MATRIX OF THE PREDICTION USING TEST DATA SET GENERATED FROM SIMULATION. ND: NO-DETECTION

Actual \ Predictions	ND	0.3	0.6	0.9
ND	0.975	0.007	0.011	0.007
0.3	0.031	0.804	0.122	0.043
0.6	0.049	0.061	0.724	0.166
0.9	0.038	0.019	0.21	0.732

Using $\gamma = 0.4$ value, the performance of the network was evaluated using the test data set, which gave precision = 0.956, recall = 0.959, and $F_1 = 0.957$. The second evaluation was performed to investigate the ability of the network to predict the correct diameter of the vessel. Table I shows the confusion matrix of this prediction. For the correctly predicted diameter, the root-mean-square errors (RMSE) of the position prediction were 0.14, 0.19, and 0.27 mm for 0.3, 0.6, and 0.9 mm vessel diameters, respectively. There were several cases where a vessel was predicted in the no-detection area state. Further analysis shows that it was in the area close to the maximum detection range of the sensor.

Finally, the network performance was evaluated using real data from insertion experiments. The insertions were performed and recorded at seven positions starting from 2.55 mm down to 0.75 mm axial distance, with 0.3 mm increments. In total, there were 160 sequences (1120 samples). The experiments were only performed for a 0.6 mm diameter vessel, with a 20 mm/s flow velocity. Fig. 5a shows an example of successive perfusion values from the insertion experiment of a vessel with a 0.67 mm off-axis distance. Fig. 5 shows the prediction probability of vessel parameters (diameter and

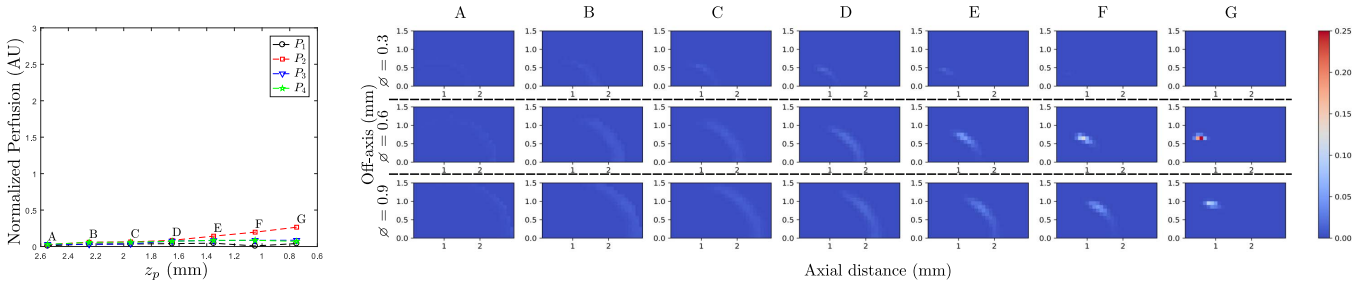

(a) (b)

Fig. 5. a) An example of insertion experiments with off-axis distance at 0.67 mm, which was used to evaluate the performance of the trained network. b) The prediction probability at instances A-G for three vessel diameters: 0.3 mm (top), 0.6 mm (middle), and 0.9 mm (bottom). The total probability of the three rows in each column, added to the probability of no-detection, is equal to 1. At the end of the insertion the actual position of the vessel was at 0.67 mm off-axis distance and 0.75 mm axial distance.

TABLE II
CONFUSION MATRIX OF THE PREDICTION USING DATA FROM INSERTION EXPERIMENTS, ND: NO-DETECTION

Actual \ Predictions	ND	0.3	0.6	0.9
ND	0.814	0.004	0.123	0.058
0.6	0.128	0.034	0.594	0.244

positions) at points A, B, C, D, E, F, and G. The first row of each column in Fig. 5 corresponds to the probability of a vessel with a diameter of 0.3 mm. The second and the third row correspond to a vessel with a diameter of 0.6 and 0.9 mm, respectively. The total prediction probability of the three rows in each column, added to the no-detection state, is equal to 1. At the end of the insertion (point G), the network correctly predicted the vessel diameter. The axial and off-axis distance predictions were 0.55 and 0.70 mm, respectively, where the actual axial distance at the end of the insertion was 0.75 mm and the actual off-axis distance was 0.67 mm.

Table II shows the confusion matrix of predictions on the vessel diameter obtained for insertion experiments data. The prediction in Table II has higher false negative and false positive rates compared to the predictions in Table I. Similar to simulation results, false negative predictions were found for the experimental data points in the area close to the maximum detection range of the sensor. Nonetheless, for the correctly predicted diameter, the position prediction RMSE was 0.18 mm, which is similar to the RMSE of simulation predictions (RMSE = 0.19 mm).

III. VESSEL DETECTION WITH MULTIPLE PROBES

In section II, an LSTM was used to predict the vessel position and diameter from successive measurements of a single probe, but the vessel's full pose in three-dimensional space remained unknown. This is because many different vessel poses can result in the same pair of off-axis and axial distances. To remove this ambiguity, in this section, the LSTM network was modified to incorporate measurements from four forward-looking laser Doppler sensors.

A. Materials and Methods

The network has the same architecture as the LSTM network described in section II-A: a two-layer LSTM with 100 LSTM cells in each layer. However, the input and the output were altered. Instead of using one perfusion value with a directional vector as an input, four perfusion values from four probes were simultaneously fetched and fed to the network. The input was presented in this form:

$$\left[Perf_{1t}\ Perf_{2t}\ Perf_{3t}\ Perf_{4t}\ \mathbf{F}^\top\right]^\top \tag{9}$$

where $Perf_{1t}, Perf_{2t}, Perf_{3t}, Perf_{4t}$ are the perfusion values for probe 1, 2, 3, 4 at time t, respectively. $\mathbf{F}^\top$ is a 3×1 vector that defines the movement direction of the probes, as described in 4.

Instead of specifying the vessel diameter and pose, in this section the network was used to predict the "no-go" area directly. To do this, firstly, the detection area of the sensors was defined (Fig. 6). As can be seen, both the needle coordinate system (x_n, y_n, z_n) and the probe coordinate system (x_p, y_p, z_p) are located at the tip of the needle. The probe coordinate system is placed at an angle of $-14.8°$ with respect to the needle coordinate system. The red-dash line in Fig. 6 shows the off-axis detection area of the sensors. At a d_{ax} distance from the probe, the off-axis detection area is a square with rounded corners. The radius of the rounded corner is equal to the maximum off-axis detection range of the sensor (det_{ax}) at that axial distance, where the side of the square (dr_{ax}) has a length of:

$$dr_{ax} = 2(d_{pn} + det_{ax}) \tag{10}$$

where d_{pn} is the distance from the probe to the y_p-axis. The position of each of the 4 probes (in the probe coordinate system) is listed in Table III. With the maximum axial detection range of the probes set at 2.4 mm, the detection volume was discretized into voxels, with the size of each voxel equal to $0.3 \times 0.3 \times 0.3$ mm. Using this voxel size, there were 1,805 voxels inside the detection range of the sensors, where each voxel was used to represent a label (class). The network was then used to predict whether a voxel is safe (it is not occupied by a vessel) or it is not safe (it is occupied by a vessel). The voxel value is set to 0 if it is safe, or 1 otherwise.

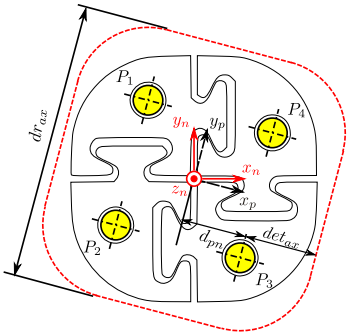

Fig. 6. The red-dash line represents the detection range of the probe in the $x_p y_p$-plane. There are two coordinate systems shown, the needle coordinate system (x_n, y_n, z_n) and probe coordinate system (x_p, y_p, z_p). P_1: probe 1; P_2: probe 2; P_3: probe 3; P_4: probe 4; d_{pn}: distance from the probe to the y_p-axis; det_{ax}: maximum off-axis detection range at a certain axial distance; dr_{ax}: detection range for the four probes.

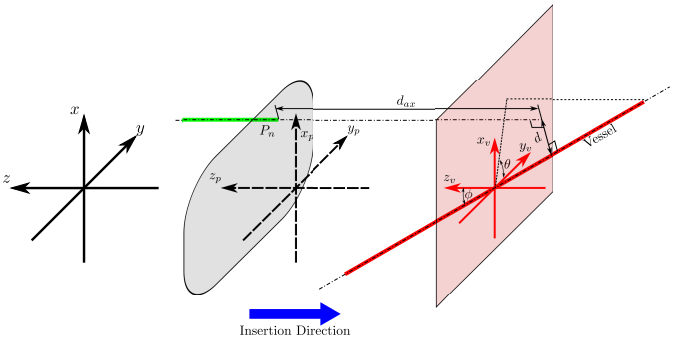

Fig. 7. Three-dimensional representation of a vessel (red line). The vessel was defined in the vessel coordinate system (x_v, y_v, z_v), with an angle of ϕ with respect to the z_v-axis. The projection of the vessel onto the $x_v y_v$-plane has an angle of θ. Probe n (P_n) is represented as a green line in the figure. During insertion, the probe coordinate system was moved along the z-axis.

TABLE III
POSITION OF LASER DOPPLER PROBES IN THE PROBE COORDINATE SYSTEM

Probe	1	2	3	4
x_p **(mm)**	-0.94	-0.94	0.94	0.94
y_p **(mm)**	0.94	-0.94	-0.94	0.94
z_p **(mm)**	0.3	0.3	0.3	0.3

Since the vessel can occupy several voxels at once, the problem becomes that of a multi-label classification, where several labels (classes) can have a value of 1. To solve the multi-label classification problem, binary relevance is used instead. Binary relevance decomposes multi-label learning into an independent binary learning problem for q number of classes [25]. The probability of each class was computed using logistic regression:

$$\sigma(z_i)_i = \frac{1}{1 + e^{-z_i}} \tag{11}$$

where $\sigma(z_i)_i$ is the probability value of class i. The class prediction was defined by:

$$h_i = \begin{cases} 0, & \text{if } \sigma(z_i)_i < 0.5 \\ 1, & \text{if } \sigma(z_i)_i \geq 0.5 \end{cases} \tag{12}$$

where h_i is the prediction for class i.

The training data set consisted of 18,000 sequences, with 30 positions in each sequence. 9,000 sequences were generated for validation, and another 9,000 for testing. To generate successive measurements for training, validation, and test data sets, the vessel was assumed to be straight within the detection range of the sensor. The vessel coordinate system $(x_v, y_v, z_v$ in Fig. 7) was used to define the orientation of the vessel, where the vessel always passes through the origin (i.e. $x_v = 0$, $y_v = 0, z_v = 0$). As can be seen in Fig. 7, the vessel has an angle of ϕ with respect to the z_v axis and the projection of the vessel in the $x_v y_v$-plane has an angle of θ. The orientation of the vessel was defined using these two angles. In the insertion simulation, the value of ϕ was randomised between 60° and 120° in 5° increments, while the value of θ was randomised between 0° and 175° in 5° increments. The vessel coordinates were then located in the global coordinate system (x, y, z). The value of the vessel coordinate in the z direction (i.e. depth) was chosen randomly to be one out of thirty possible ones ($z = 0$ to $z = -8.7$ mm in 0.3 mm decrements). For $\theta \neq 90°$, the location of the vessel coordinate in the x direction was set to 0, while the location in the y direction was chosen randomly between -2 and 2 mm, in 0.2 mm increments. For $\theta = 90°$, the y position was set at 0 while the x position was randomised between -2 and 2 mm in 0.2 mm increments. At the beginning of the insertion, the probe coordinate system $(x_p, y_p, z_p$ in Fig. 7) was located at the origin of the global coordinate system ($x = 0, y = 0, z = 0$). The probe (green line in Fig. 7) was located at a fixed position in the probe coordinate system. The probe coordinate system was then moved forward in 0.3 mm increments. If the z position of the probe coordinate system was less than the z position of the vessel coordinate system, one out of three options was chosen for the next step until the 29^{th} step was reached: move backwards, stop or move forwards. The value of class i was set to 1 if the distance from the voxel in the global coordinate system to the vessel was less than the vessel diameter. The axial distance (d_{ax}) and off-axis distance (d) from the probe to the vessel were calculated using the simple line-to-line distance [26].

In the multi-label classification, the imbalance in the dataset was evaluated in each class using [27]:

$$ImR_i = \frac{\max(|\mathcal{D}_i^+|, |\mathcal{D}_i^-|)}{\min(|\mathcal{D}_i^+|, |\mathcal{D}_i^-|)} \tag{13}$$

where ImR_i is the imbalance ratio of class i, $|\mathcal{D}_i^+|$ is the total number of relevant values (the value of the class is 1) of class i, and $|\mathcal{D}_i^-|$ is the total number of irrelevant values (the value of the class is 0) of class i in the training data sets. The average imbalance ratio (ImR) is:

$$ImR = \frac{1}{q}\sum_{i=1}^{q} ImR_i \tag{14}$$

where q is the total number of classes. Usually the number of relevant values in the data sets is less than the number of irrelevant values. During training, the cost of misclassification

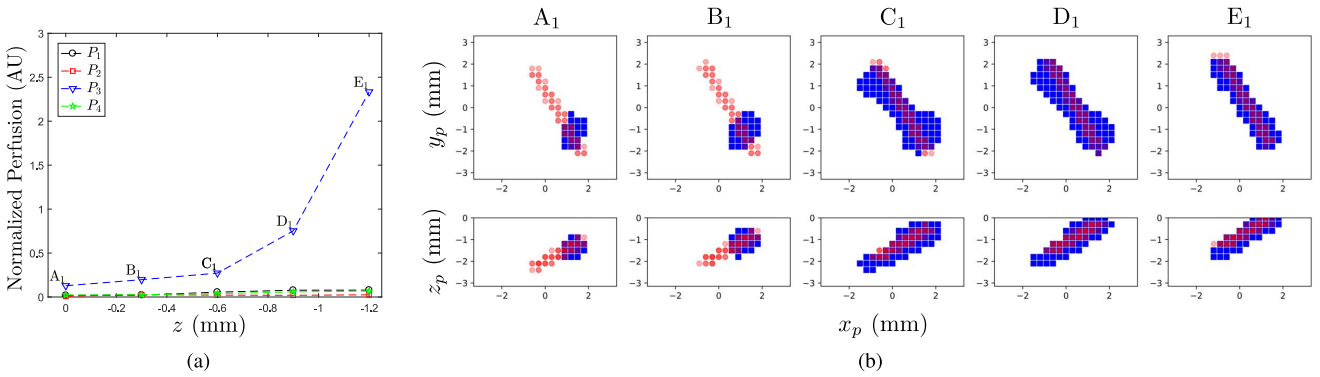

Fig. 8. a) An example of simulated perfusion values for a vessel located at $x = 0, y = 0.8, z = -1.8$ mm, with $\theta = 120°$ and $\phi = 75°$. b) Projection of the actual (red-circles) and predicted (blue-squares) vessel area inside the detection area of the sensors on the $x_p y_p$- (top) and on the $x_p z_p$- (bottom) planes, with corresponding perfusion values (Points A_1 - E_1).

of relevant values (C) was increased by:

$$C = (ImR)^{\gamma_m} \tag{15}$$

where, as described in section II-A, $\gamma_m \in [0, 1]$ is a trade-off parameter. Using the same method as in Section II-A, we then chose $\gamma_m = 0.4$.

As in the previous section, the trained network was evaluated using precision, recall, the F_1-score, and Hamming loss. The Hamming loss evaluates the fraction of misclassified prediction-label pairs [28]. Since Hamming loss is a loss function, the lower the hamming loss, the better the network performance. Since the detection area in Fig. 6 was based on the maximum detection area for a 0.9 mm diameter vessel, the evaluation was only conducted if there was enough information from the perfusion value to define the "no-go" area of the vessel (i.e. the perfusion value from at least one of the four probes was not in the no-detection state). The trained network was then used to predict the "no-go" area for real insertion experiments. In the experiments, a vessel phantom 0.6 mm in diameter and a flow velocity of 20 mm/s, was used. In the needle coordinate system, the vessel is at $\phi = 90°$ and $\theta = 0°$. Vessel orientation was then transformed into the probe coordinate system. Details for the experiments are those previously described in [17].

B. Results

In the test data set generated from simulation, the network perfomed as follows: precision = 0.43, recall = 0.78, F_1-score = 0.56, Hamming loss = 0.035. Fig. 8 shows an example of the network's ability to predict the presence and pose of a vessel that was not in a plane perpendicular to the needle insertion axis. The vessel coordinate system was located at $x = 0, y = 0.8, z = -1.8$ mm. The orientation of the vessel was set at $\theta = 120°$ and $\phi = 75°$. The successive perfusion values (A_1 to E_1 in Fig. 8a) were generated using simulation by moving the probe coordinate system from $z = 0$ to $z = -1.5$ in 0.3 mm decrements. The blue area in Fig. 8b shows voxels that were predicted to be occupied by the vessel. The red circles in Fig. 8b represent actual voxels occupied by the vessel. To ease comparison, the voxels were projected in the $x_p y_p$-plane (Fig. 8b top) and $x_p z_p$-plane (Fig. 8b bottom). Starting from Point C_1, the network predicted the vessel orientation and position correctly.

The network was then used to predict the "no-go" area based on data from real insertion experiments. In total, there were 40 insertion experiments with each experiment consisting of seven sequences (total number of samples = 280). Fig. 5a shows the the perfusion values for the four probes while the probes were advancing toward the vessel at seven example positions (A_0 - G_0). The vessel was located at $z = -2.25$, $x = 0, y = -0.2$ mm. Again, the red circles represent voxels where the vessel was located, while the blue squares highlight voxels predicted to contain the vessel. At the start (Point A_0), the vessel was inside the detection volume of the sensor; however, the network did not predict this. As explained in section III-A, the reason for the missed detection relates to the fact that the detection volume of the sensor was defined with the maximum detection range for a 0.9 mm vessel. At Point A_0, the vessel location was still out of the the detection range of the probes for a 0.6 mm diameter vessel. Prediction of the vessel pose, however, is shown to improve with each successive measurement, where, at the end of the insertion (Point G_0), the entire vessel volume is correctly predicted. The prediction evaluation metrics for the experiments were found to be: precision = 0.21, recall = 0.54, F_1-score = 0.30, and Hamming loss = 0.078. It should be noted that, if the evaluation metrics were performed only at Point G_0, the recall value would increase to 0.77, which means a 77% prediction accuracy full vessel volume estimation at Point G_0.

IV. Discussion

In section II, an LSTM network was used to predict a vessel diameter and position based on successive measurements from a single probe. The confusion matrix in Table I shows that, in addition to false negatives, there was vessel diameter misclassification as well. The diameter misclassification was predominantly between two classes with a small diameter difference. The misclassification of vessels with a diameter of 0.6 mm into a 0.9 mm diameter vessel, however, was higher compared to misclassification into a 0.3 mm diameter vessel. The reason for this may be because of the probe's detection range for a 0.6 mm diameter vessel being closer to the probe's

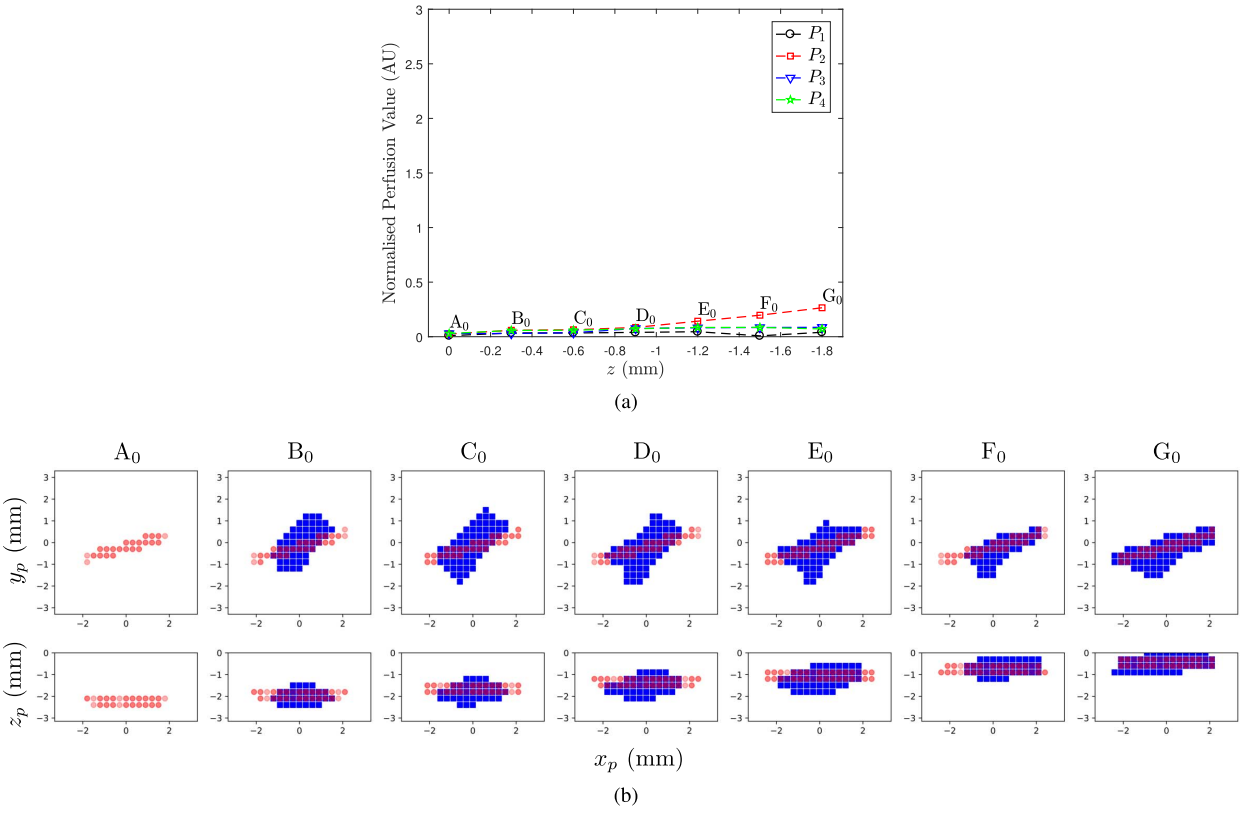

Fig. 9. a) Example perfusion values from the insertion experiments. The measurements were taken while the needle was located at $z = 0$ to $z = -1.8$ mm, in 0.3 mm decrements; b) Projection of the actual (red-circles) and predicted (blue-squares) vessel area inside the detection area of the sensors on the $x_p y_p$- (top) and on the $x_p z_p$- (bottom) planes, with corresponding perfusion values (Points A_0 - G_0).

detection range for a vessel which is 0.9 mm in diameter (Fig. 3). It should be noted that, here, all vessel diameters were assumed to have the same range of flow velocity rates (10 - 20 mm/s). In future work, the flow velocity range for each vessel diameter could be assigned a different set of values [29] that should be easier for the network to discriminate between.

Even though it is possible to incorporate the prediction achieved with a single probe into the algorithms presented in [16], [17], the assumption that the vessel is in a plane perpendicular to the needle insertion axis might limit its applicability. Therefore, in Section III, another LSTM network was trained to predict the vessel pose directly. As can be seen in Fig. 9, the prediction improves as the needle approaches the vessel. This means that, in order to obtain more information about the vessel pose, the insertion may need to continue once a vessel is first detected. Since the prediction area provides information about the position of the vessel in the z_p direction when the vessel is first detected (Point B_0 in Fig. 9), the maximum insertion length that is required to acquire more vessel information can be determined, as to avoid inadvertent vessel damage.

Here, a binary relevance method was used for multi-label learning of an LSTM network, which shows good prediction results. However, binary relevance lacks any label correlation [25]. To incorporate label correlation, another network architecture that performs better with spatial and temporal data, such as convolutional LSTM network, might be used [30].

The goal of vessel detection in a steerable needle system is to generate a "no-go" area in front of the needle, which can be used to plan and execute an escape procedure. In section III, the "no-go" area was defined while all of the segments were aligned. Since the PBN is steered by introducing an offset between segments, if the leading segment/s detects a vessel, all of the probes need to be aligned to predict the "no-go" area appropriately. The detection method in Section III, however, can still be executed by storing the position information so that the perfusion measurements from each probe can be sorted according to position, thus avoiding this additional step.

The results from section II and III show that the network can predict information about the vessel even though the optical properties of the tissue differ within a range (μ_s' : 0.75 ± 0.2 mm^{-1}). If the optical properties vary significantly, for example when at the interface between grey matter and white matter, the network may be unable to identify a generalization. However, since the tissue greyness can be observed using a laser Doppler system based on the intensity of the detected light [11], light intensity could be added as a further network input to differentiate between white and grey matter. Also, the total light intensity could be used to detect the presence of a blood vessel [12], [13]. With this additional input, we believe that the prediction accuracy could be improved.

Even though the networks were trained using simulation data, the results show that these can be used to predict experimental measurements correctly. Use of the simulation

data sped up the training process for different probes and needle properties (e.g. LDF with a different wavelength, different needle sizes, different probe configurations, etc.). Consequently, real insertion experiments could be performed in the evaluation stage only, resulting in significant time and effort gains. In principle, it would be possible to incorporate the experimental data in the training step to improve prediction accuracy, albeit the size of any experimental dataset will never be as large as the simulation data, which may cause bias. We could however use the former to fine-tune the network through a transfer learning algorithm [31], which will be part of our future works.

In this article, the vessel was assumed to be static. Previously, a high-resolution material tracking set-up based on Particle Image Velocimetry (PIV) was used to investigate tool-tissue interactions [32]. By combining this method with a vessel embedded within the sample, the movement of the vessel during insertion could be predicted. This movement prediction could then be applied in the simulation so that the LSTM network would take into account the effect of vessel movement.

V. Conclusion

In this article, LSTM networks have been used to predict the vessel diameter and position based on successive Laser Doppler Flowmetry measurements from a single probe and to predict the full vessel pose based on simultaneous measurements from four probes embedded in a prototype PBN. The single probe LSTM network is essential to detect the presence of a vessel while an offset is introduced between segments to steer, as it will work regardless of which segment approaches the vessel first. In this configuration, the network could classify the vessel diameter for unknown vessel and tissue properties with an accuracy of 75%. For the correctly predicted diameter, the position could then be accurately predicted with sub-millimetre accuracy (0.27 mm). Once a vessel is detected, all segments are aligned and all probe measurements are used to estimate the complete pose of an approaching vessel, to avoid collision and plan an eventual avoidance strategy. In these experiments, the network could predict the pose of the vessel after a few successive measurements were acquired, with an average 77% final overlap between actual and predicted vessel volumes. In doing so, the no-go volume detected in front of the needle captures the full information about the vessel's pose and diameter, showing a significant improvement over the algorithms developed in previous works [16], [17].

References

[1] M. R. Proctor and P. M. Black, *Minimally Invasive Neurosurgery*. Totowa, NJ, USA: Humana Press, 2005.

[2] D. Pinggera *et al.*, "Serious tumor seeding after brainstem biopsy and its treatment—A case report and review of the literature," *Acta Neurochirurgica*, vol. 159, no. 4, pp. 751–754, 2017.

[3] A. W. Shukla and M. S. Okun, "State of the art for deep brain stimulation therapy in movement disorders: A clinical and technological perspective," *IEEE Rev. Biomed. Eng.*, vol. 9, pp. 219–233, 2016.

[4] N. U. Barua, S. S. Gill, and S. Love, "Convection-enhanced drug delivery to the brain: Therapeutic potential and neuropathological considerations," *Brain Pathol.*, vol. 24, no. 2, pp. 117–127, 2014.

[5] I. J. Gerard, M. Kersten-Oertel, K. Petrecca, D. Sirhan, J. A. Hall, and D. L. Collins, "Brain shift in neuronavigation of brain tumors: A review," *Med. Image Anal.*, vol. 35, pp. 403–420, Jan. 2017.

[6] C.-H. Huang *et al.*, "High-resolution structural and functional assessments of cerebral microvasculature using 3d gas δr2*-mmra," *PloS ONE*, vol. 8, no. 11, 2013, Art. no. e78186.

[7] A. J. Fenoy and R. K. Simpson, Jr., "Risks of common complications in deep brain stimulation surgery: Management and avoidance," *J. Neurosurgery*, vol. 120, no. 1, pp. 132–139, 2014.

[8] C.-P. Liang *et al.*, "A forward-imaging needle-type OCT probe for image guided stereotactic procedures," *Opt. Express*, vol. 19, no. 27, pp. 26283–26294, 2011.

[9] H. Ramakonar *et al.*, "Intraoperative detection of blood vessels with an imaging needle during neurosurgery in humans," *Sci. Adv.*, vol. 4, no. 12, Dec. 2018, Art. no. eaav4992.

[10] C.-P. Liang *et al.*, "Coherence-gated Doppler: A fiber sensor for precise localization of blood flow," *Biomed. Opt. Express*, vol. 4, no. 5, pp. 760–771, 2013.

[11] K. Wårdell, S. Hemm-Ode, P. Rejmstad, and P. Zsigmond, "High-resolution laser Doppler measurements of microcirculation in the deep brain structures: A method for potential vessel tracking," *Stereotactic Funct. Neurosurgery*, vol. 94, no. 1, pp. 1–9, 2016.

[12] F. Picot *et al.*, "Interstitial imaging with multiple diffusive reflectance spectroscopy projections for *in vivo* blood vessels detection during brain needle biopsy procedures," *Neurophotonics*, vol. 6, no. 2, Apr. 2019, Art. no. 025003.

[13] N. A. Markwardt *et al.*, "Remission spectrometry for blood vessel detection during stereotactic biopsy of brain tumors," *J. Biophotonics*, vol. 10, no. 8, pp. 1080–1094, 2017.

[14] L. Frasson, F. Ferroni, S. Y. Ko, G. Dogangil, and F. R. Y. Baena, "Experimental evaluation of a novel steerable probe with a programmable bevel tip inspired by nature," *J. Robotic Surg.*, vol. 6, no. 3, pp. 189–197, 2012.

[15] T. Watts, R. Secoli, and F. R. y Baena, "A mechanics-based model for 3-D steering of programmable bevel-tip needles," *IEEE Trans. Robot.*, vol. 35, no. 2, pp. 371–386, Apr. 2019.

[16] V. Virdyawan, M. Oldfield, and F. R. y Baena, "Laser Doppler sensing for blood vessel detection with a biologically inspired steerable needle," *Bioinspiration Biomimetics*, vol. 13, no. 2, 2018, Art. no. 026009.

[17] V. Virdyawan and F. R. y Baena, "Vessel pose estimation for obstacle avoidance in needle steering surgery using multiple forward looking sensors," in *Proc. IEEE/RSJ Int. Conf. Intell. Robots Syst. (IROS)*, Oct. 2018, pp. 3845–3852.

[18] F. D. de Mul *et al.*, "Laser Doppler velocimetry and Monte Carlo simulations on models for blood perfusion in tissue," *Appl. Opt.*, vol. 34, no. 28, pp. 6595–6611, 1995.

[19] F. F. M. de Mul, "Monte Carlo simulation of light transport in turbid media," in *Handbook of Coherent Domain Optical Methods*, V. Tuchin, Ed. New York, NY, USA: Springer, 2012, pp 593–661.

[20] M. Larsson, W. Steenbergen, and T. Stroemberg, "Influence of optical properties and fiber separation on laser Doppler flowmetry," *J. Biomed. Opt.*, vol. 7, no. 2, pp. 236–243, Apr. 2002.

[21] Z. C. Lipton, J. Berkowitz, and C. Elkan, "A critical review of recurrent neural networks for sequence learning," May 2015, *arXiv:1506.0001*. [Online]. Available: https://arxiv.org/abs/1506.00019

[22] N. Reimers and I. Gurevych, "Optimal hyperparameters for deep LSTM-networks for sequence labeling tasks," Jul. 2017, *arXiv:1707.06799*. [Online]. Available: https://arxiv.org/abs/1707.06799

[23] W. Zaremba, I. Sutskever, and O. Vinyals, "Recurrent neural network regularization," Sep. 2014, *arXiv:1409.2329*. [Online]. Available: https://arxiv.org/abs/1409.2329

[24] D. Tran, H. Mac, Van Tong, H. A. Tran, and L. G. Nguyen, "A LSTM based framework for handling multiclass imbalance in DGA botnet detection," *Neurocomputing*, vol. 275, pp. 2401–2413, Jan. 2018.

[25] M.-L. Zhang, Y.-K. Li, X.-Y. Liu, and X. Geng, "Binary relevance for multi-label learning: An overview," *Frontiers Comput. Sci.*, vol. 12, no. 2, pp. 191–202, 2018.

[26] E. W. Weisstein. (2002). *Line-Line Distance*. Aug. 13, 2018. [Online]. Available: http://mathworld.wolfram.com/Line-LineDistance.html

[27] M.-L. Zhang, Y.-K. Li, and X.-Y. Liu, "Towards class-imbalance aware multi-label learning," in *Proc. 24th Int. Joint Conf. Artif. Intell. (IJCAI)*, Jun. 2015, pp. 4041–4047.

[28] M.-L. Zhang and Z.-H. Zhou, "A review on multi-label learning algorithms," *IEEE Trans. Knowl. Data Eng.*, vol. 26, no. 8, pp. 1819–1837, Aug. 2014.

[29] S. K. Piechnik, P. A. Chiarelli, and P. Jezzard, "Modelling vascular reactivity to investigate the basis of the relationship between cerebral blood volume and flow under CO_2 manipulation," *NeuroImage*, vol. 39, no. 1, pp. 107–118, 2008.

[30] X. Shi, Z. Chen, H. Wang, D.-Y. Yeung, W.-K. Wong, and W.-C. Woo, "Convolutional LSTM network: A machine learning approach for precipitation nowcasting," in *Proc. Adv. Neural Inf. Process. Syst.*, 2015, pp. 802–810.
[31] K. Bousmalis *et al.*, "Using simulation and domain adaptation to improve efficiency of deep robotic grasping," in *Proc. IEEE Int. Conf. Robot. Automat. (ICRA)*, May 2018, pp. 4243–4250.
[32] A. Leibinger, M. J. Oldfield, and F. R. y Baena, "Minimally disruptive needle insertion: A biologically inspired solution," *Interface Focus*, vol. 6, no. 3, 2016, Art. no. 20150107.

Vani Virdyawan received the B.Sc. and M.Sc. degrees in mechanical engineering from the Institut Teknologi Bandung, Indonesia, in 2010 and 2011, respectively, and the Ph.D. degree in medical robotics from Imperial College London, U.K., in 2018.

He is currently a Research Associate with the Mechatronics in Medicine Laboratory, Imperial College London, U.K. His research interests include laser-based sensors, machine learning, and surgical robotics.

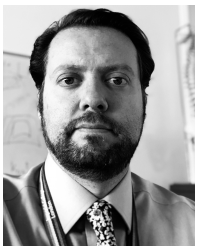

Ferdinando Rodriguez y Baena graduated with the First Class Honors degree in mechatronics and manufacturing systems engineering from King's College London in 2000 and received the Ph.D. degree in medical robotics from Imperial College in 2004.

He is a Professor of Medical Robotics with the Department of Mechanical Engineering, Imperial College, where he leads the Mechatronics in Medicine Laboratory. He is also the Mechanical Engineering Postgraduate Tutor, and the current Speaker for the Imperial College Robotics Forum. He has published over 150 papers and has secured in excess of £12M in research funding to date. His current research interest includes application of mechatronic systems to medicine, in the specific areas of clinical training, diagnostics, and surgical intervention. His team has a strong translational focus, while his work encompasses both "blue skies" research and "near-to-market" development.

Prof. Rodriguez y Baena was an Associate Editor for the *IEEE Robotics and Automation Magazine*. He is the Chair of the Program Committee for the International Society for Computer Assisted Orthopaedic Surgery, the International Workshop on Medical Robotics and the Joint Workshop on New Technologies for Computer/Robot Assisted Surgery, and the IET's Communities Committee for Technical and Professional Networks. He was a Leverhulme Prize winner (engineering), a former ERC Grant holder, and the coordinator of an £8.3M European project on robotic-assisted neurosurgical drug delivery.